Article

Effect of Ruthenium Modification of g-C$_3$N$_4$ in the Visible-Light-Driven Photocatalytic Reduction of Cr(VI)

Truong Nguyen Xuan [1], **Dien Nguyen Thi** [1], **Tue Nguyen Ngoc** [1], **Khanh Dang Quoc** [2], **Miklós Németh** [3], **Shoaib Mukhtar** [4] **and Ottó Horváth** [4,*]

[1] School of Chemical Engineering, Hanoi University of Science and Technology, No.1 Dai Co Viet Street, Hai Ba Trung Distric, Hanoi 100000, Vietnam; truong.nguyenxuan@hust.edu.vn (T.N.X.); dien.nt212318m@sis.hust.edu.vn (D.N.T.); tue.nguyenngoc@hust.edu.vn (T.N.N.)

[2] School of Materials Science and Engineering, Hanoi University of Science and Technology, No.1 Dai Co Viet Street, Hai Ba Trung Distric, Hanoi 100000, Vietnam; khanh.dangquoc@hust.edu.vn

[3] Centre for Energy Research, Surface Chemistry and Catalysis Department, Konkoly-Thege Street 29-33, H-1121 Budapest, Hungary; nemeth.miklos@ek-cer.hu

[4] Research Group of Environmental and Inorganic Photochemistry, Center for Natural Sciences, Faculty of Engineering, University of Pannonia, P.O. Box 1158, H-8210 Veszprém, Hungary; shoaibmukht131@gmail.com

[*] Correspondence: horvath.otto@mk.uni-pannon.hu; Tel.: +36-88-624-000 (ext. 6049)

Abstract: Graphitic carbon nitride (g-C$_3$N$_4$) is a promising heterogeneous photocatalyst in the visible range. It can be used, among others, for reductive conversion of the toxic hexavalent chromium occurring in various wastewaters. Its photocatalytic efficiency, however, has to be improved, which can be realized by modification with different dopants or co-catalysts forming heterojunctions. In our work, ruthenium-modified g-C$_3$N$_4$ has been prepared by ultrasonic impregnation of the pristine g-C$_3$N$_4$, which was synthesized from thiourea. The morphology, microstructure, and optical properties of the photocatalysts were characterized by XRD, SEM, FT-IR, TEM, XPS, and DRS. Their compositions were analyzed by EDS and XPS measurements, indicating 0.5% and 1.4% Ru, due to the different penetrating depths. XPS study showed mainly +2 for the oxidation state of Ru. DRS analysis indicated a slight change in both the CB (from -1.14 to -1.22 eV) and the VB (from 1.49 to 1.56 eV) energies of Ru/g-C$_3$N$_4$, compared to those of g-C$_3$N$_4$. The photocatalytic Cr(VI) reduction efficacy increased from 50.1 to 96.8%. Low pH (=2) was preferred for the photocatalytic Cr(VI) reduction due to the favorable surface charge and E(Cr(VI)/Cr(III)) redox potential. Ru modification proved to be promising for improving the photocatalytic performance of g-C$_3$N$_4$.

Keywords: graphitic carbon nitride; photocatalysis; ruthenium modification; reduction of Cr(VI); visible-light-irradiation; pH effect

1. Introduction

Heterogeneous photocatalysis became an intensively developing field of science in past decades because it offers good possibilities for the removal of various types of pollutants [1]. In several cases, for this purpose, utilization of solar radiation can also be realized by photoactive semiconductors. Unfortunately, a significant part of the stable and efficient heterogeneous photocatalysts are white (such as TiO$_2$, SnO$_2$, ZnO), and thus they can only be excited in the UV range [2], which represents only a low fraction of the solar light. Hence, more and more interest has been attracted by colored semiconductors, a considerable part of which is organic. The advantage of organic semiconductors (OSCs) is that their basic structure is metal-free, which is important from the viewpoint of environmental protection, and they are relatively easy to prepare in rather mild experimental conditions. One of the most promising OSCs is graphitic carbon nitride (g-C$_3$N$_4$), which is a conjugated polymer [3]. It is suitable for efficient utilization of the longer-wavelength photons due to

its band gap corresponding to an energy of 2.7–2.8 eV, which falls in the visible light range. However, this narrow visible light response (up to c.a. 450 nm) and fast recombination of the photogenerated charge carriers are considerable drawbacks of this photocatalyst [4]. For enhancing the efficiency of this photocatalyst, "heterojunction"-type structures offer good possibilities. Numerous studies have applied various materials for such combinations, e.g., other semiconductors [5,6], metals [7,8], and non-metals [9,10] as dopants. These modified g-C_3N_4 semiconductors have been applied for both photocatalytic oxidation and the reduction of various substrates, e.g., for water splitting [11,12], CO_2 reduction [13], and the degradation of organic pollutants [14].

One of the reducing photocatalytic procedures applied for the removal of pollutants in various wastewaters focuses on the Cr(VI) conversion to Cr(III). Inorganic chromium compounds are widely used in various industries such as electroplating, leather and dye manufacturing, metal processing, etc. [15,16] Chromium occurs mostly in two forms: hexavalent and trivalent chromium (Cr(VI) and Cr(III)). The former is much more soluble (hence, mobile) and poisonous (carcinogenic) than the latter form. Therefore, the removal of chromium is basically focused on Cr(VI) due to its severe health issues. Accordingly, g-C_3N_4 has also been investigated in this respect without modification, but prepared from different precursors [17]. Several studies dealt with the photocatalytic reduction of Cr(VI) to Cr(III) based on the application of this semiconductor modified in various ways. Acid-base regulation was utilized for its surface modification [18]. Decoration with Ag nanoclusters was also applied for enhancing the reduction efficiency [19]. Combination with reduced graphene oxide and CoS_2 also proved promising [20]. The $Cu_{3.21}Bi_{4.79}S_9$/g-C_3N_4 nanocomposite was also used under visible light irradiation for this purpose, even in the presence of other heavy metal ions [21]. The degradation of organic pollutants was combined with the Cr(VI) reduction in the Z-scheme system consisting of a g-C_3N_4 /Bi_2S_3 heterojunction [22]. In the composite of g-C_3N_4/$ZnIn_2S_4$, the improved charge separation was the possible reason for the increased efficiency [23]. The same explanation, along with the larger specific surface area, was the interpretation of the higher efficacy of the illite-g-C_3N_4 catalyst [24]. The combination of g-C_3N_4 with Cu_2O also led the increased reduction and, at the same time, the oxidation potentials utilized for reductive conversion of Cr(VI) and oxidative degradation of tetracycline [25].

The previous results regarding the g-C_3N_4-based photocatalytic reduction of Cr(VI) clearly indicated that several types of modifications can improve the efficiency of this process. However, despite the wide range of studies, the effect of the modification with ruthenium has not been investigated on the Cr(VI) conversion, although this metal proved to be a useful dopant in the case of other photoactive semiconductors. Hence, the main goal of our study was the preparation and characterization of ruthenium-modified g-C_3N_4 (designated as Ru/g-C_3N_4), and its application for the photocatalytic reduction of Cr(VI), compared to the pristine g-C_3N_4. Optimization of the photocatalytic conditions (e.g., pH, concentrations) as well as stability measurements were also realized. Our results clearly indicate that ruthenium modification resulted in an improved photocatalytic performance regarding the Cr(VI) conversion, and its efficiency hardly changed through several reusing cycles.

2. Results and Discussion

2.1. Structure and Properties Characterization

2.1.1. XRD Analysis

The XRD patterns of prepared Ru/g-C_3N_4 and g-C_3N_4 catalysts are shown in Figure 1. The XRD patterns demonstrate that Ru/g-C_3N_4 maintains the crystal characteristic of pristine porous g-C_3N_4. The weak peak appeared at 13.08° and the strong one situated at 27.56° are ascribed to the (100) and (002) planes of g-C_3N_4 (JCPDS No. 87-1526), respectively [26]. Characteristic peaks at 27.56° are assigned to the dense interlayer-stacking (002) peak of aromatic segments of g-C_3N_4 materials. The (002) diffraction of the carbon in Ru/C indicates that it has a quasi-graphitic structure. The reflection at 13.08° is indexed

as (100) peak that arises from the in-plane ordering of tri-s-triazine attributed to units of g-C$_3$N$_4$. This means that the loading of Ru did not change the basic structure of g-C$_3$N$_4$. The absence of an apparent characteristic peak of Ru on Ru/g-C$_3$N$_4$ indicates that Ru has a small particle size, low loading, and good dispersion on the g-C$_3$N$_4$ surface. The decreased intensity of the characteristic peaks in the XRD patterns of Ru/g-C$_3$N$_4$ may be attributed to a reduced layer thickness caused by Ru doping [27].

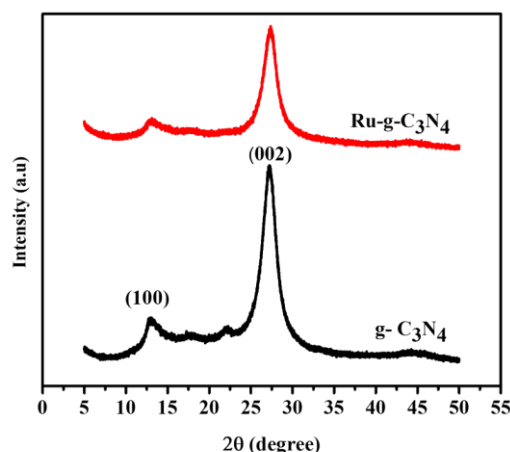**Figure 1.** XRD patterns of g-C$_3$N$_4$ and the Ru/g-C$_3$N$_4$ catalysts.

2.1.2. UV–Vis Spectroscopic Study

Absorption spectroscopy is used to determine the optical properties of the synthesized samples, which is an important factor for photocatalysts. Figure 2 shows the DR/UV–Vis diffuse reflectance spectra and the Kubelka–Munk plot [28] of the sample's Ru/g-C$_3$N$_4$ and g-C$_3$N$_4$. The significant decrease in the reflection upon Ru doping (Figure 2a) can be attributed to the enhanced light absorption, which is in accordance with the much darker color.
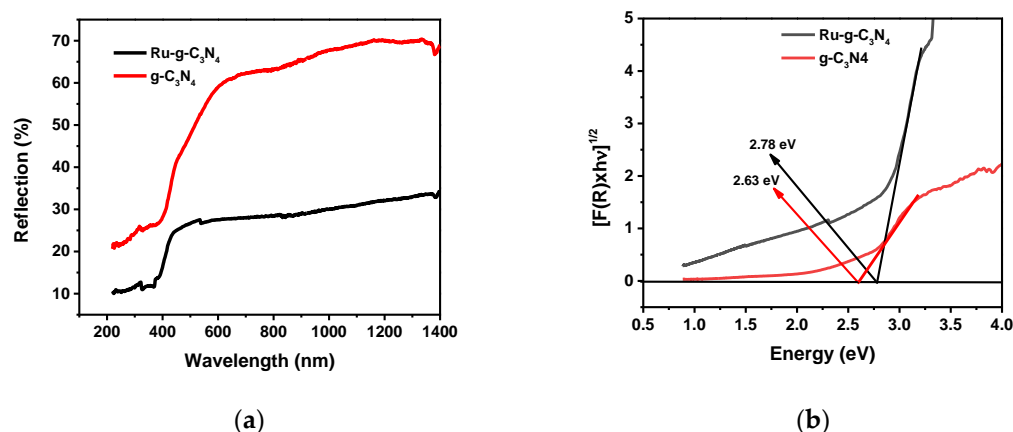

(**a**) (**b**)

Figure 2. (**a**) DR/UV–Vis spectra, (**b**) energy bandgap determination by the Kubelka–Munk function for the catalysts: g-C$_3$N$_4$ and Ru/g-C$_3$N$_4$.

Absorption in the visible light range (from 400 to 750 nm) is an important condition for the photocatalytic activity of g-C$_3$N$_4$ under visible light. When doping Ru NPs onto the material, an increased band gap (Eg) from 2.63 to 2.78 eV was determined (Table 1), corresponding to the blue shift of the absorption edge from 471 nm (g-C$_3$N$_4$) to 446 nm Ru/g-C$_3$N$_4$). However, both the g-C$_3$N$_4$ and Ru/g-C$_3$N$_4$ composites showed absorption in the visible region, corresponding to the transition from the valence band (VB) to the conduction band (CB).

Table 1. The calculated conduction band (ECB) and valence band (EVB) energies.

Catalyst	E_g (eV)	E_{VB} (eV)	E_{CB} (eV)
g-C_3N_4	2.63	1.49	-1.14
Ru/g-C_3N_4	2.78	1.56	-1.22

The E_{VB} and E_{CB} values were estimated by adopting the Mulliken electronegative principle, using Equations (1) and (2):

$$ECB = EVB - Eg \tag{1}$$

$$EVB = \chi - Ee + 0.5Eg \tag{2}$$

where χ represents Mulliken electronegative symbol of g-C_3N_4 (4.67 eV) and E_e is the energy of free electrons on the hydrogen scale ($E_e \approx 4.50$ eV).

In this calculation, for both g-C_3N_4 and Ru/g-C_3N_4, the same electronegativity (χ) was taken because Ru doping (with 1.4% surface concentration) could just slightly modify it. This estimation resulted in an E_{CB} value for this semiconductor which is more negative than that of g-C_3N_4. The obtained E_{CB} values hardly differ, which results in an equilibrium of the electrons between the two CBs. Nevertheless, it can promote some capturing of the electrons from the CB of g-C_3N_4, which can be excited easier than Ru/g-C_3N_4. Thus, the charge recombination in the previous one becomes more hindered. The slightly more negative CB potential of the ruthenium-modified semiconductor favors the reduction of Cr(VI).

2.1.3. SEM and EDS Analysis

The morphology of g-C_3N_4 consists of large sheet-like layers with folds and voids on the surface (Figure 3a). After adding the ruthenium (presumably RuO_x) nanoparticles, on the samples of Ru/g-C_3N_4 composites appeared some nanoparticles agglomerated on the surface of g-C_3N_4, leading to the formation of a heteromorphic structure; in addition, the pore size was narrowed due to the covering of ruthenium on g-C_3N_4 (Figure 3b).

(**a**)   (**b**)
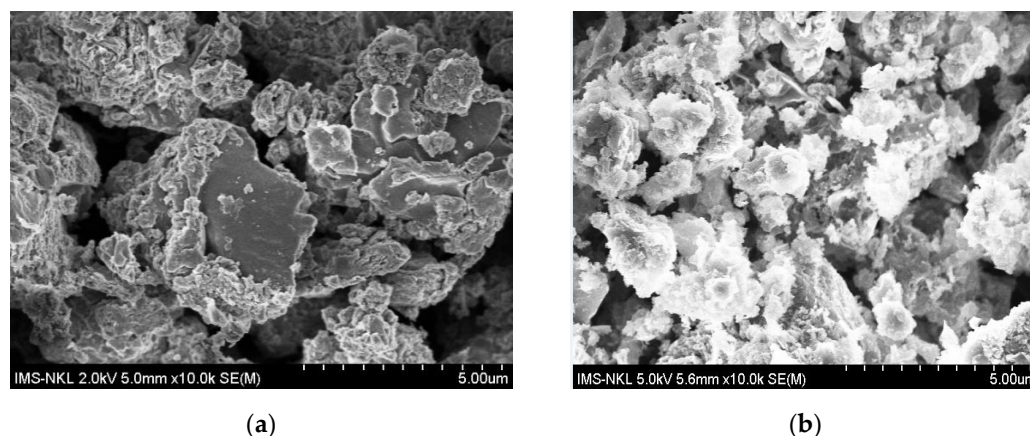
Figure 3. SEM images of catalyst materials (**a**) g-C_3N_4 and (**b**) Ru/g- C_3N_4.

In addition, the results of the EDS analysis (Figure 4) also confirmed the presence of ruthenium on the surface of g-C_3N_4 material. The elemental composition of the compound Ru/g-C_3N_4 synthesized from energy dispersive spectroscopy (EDS) shows that the compound contains 21.56% C, 3.21% O, 74.73% N, and 0.5% Ru.
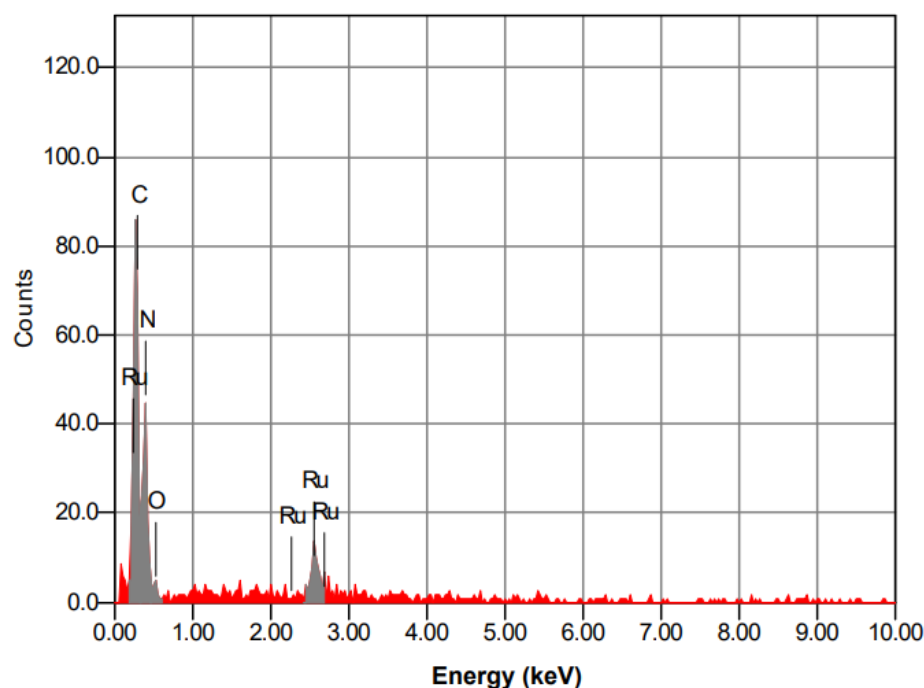
Figure 4. EDS spectrum of Ru-g-C$_3$N$_4$ material.

2.1.4. FT-IR Analysis

Figure 5 is the FT-IR spectrum of samples g-C$_3$N$_4$ and Ru/g-C$_3$N$_4$. The characteristic absorption fringes at 3100 cm^{-1} on the IR spectra of g-C$_3$N$_4$ and Ru-g-C$_3$N$_4$, respectively, are assigned to the valence oscillations of N-H [29]. Absorption fringes at about 1637 cm^{-1} and 1242 cm^{-1} can be attributed to the fluctuations of the C-N, C=N valences of the aromatic heterocyclic [30]. The intense bands at 1637, 1572, 1409, and 1242 cm^{-1} were assigned to typical stretching vibration modes of triazine-derived repeating units Finally, the strong absorption fringes at 810 cm^{-1} in the g-C$_3$N$_4$ and Ru/g-C$_3$N$_4$ samples, respectively, characterize the oscillation of the s-triazine ring absorption band. Furthermore, there is no absorption pattern associated with sulfur bonds (such as –SH, –SN, –SC), demonstrating that elemental sulfur is completely liberated during heat treatment [31]. A similar mode vibration was also present in Ru/g-C$_3$N$_4$, clearly indicating all modes of vibration preservation after ruthenium incorporation and without disturbing the typical molecular structure of g-C$_3$N$_4$.

2.1.5. XPS Analysis

XPS spectroscopy was employed to check the surface compositions as well as chemical state of the elements present in g-C$_3$N$_4$ and Ru/g-C$_3$N$_4$.

Accordingly, C1s spectrum shows four characteristic peak components at 293.4, 288.2, 286.7, and 285.1 eV corresponding to plasmon excitation of the heptazine heterocycles, sp^2-bonded carbon (N–C=N), C–O, and C–C bonds [32,33], respectively, in both the prepared g-C$_3$N$_4$ and Ru/g-C$_3$N$_4$ material (Figure 6a,b). It demonstrates that the structure of g-C$_3$N$_4$ remains after synthesis.

For the Ru/g-C$_3$N$_4$ catalyst, the C 1s/Ru 3d region has a complex structure indicating a clear peak at 281.8 eV (Figure 6b), which can be assigned—in conjunction with the Ru 3p3/2 peak at 463.3 eV (Figure 6d)—to the Ru(II)–nitrogen bond [34–37].

The N1s spectra can be deconvoluted into four individual peaks at about 398.7, 400.0, 401.2, and 404.9 eV (Figure 6e). The peak at about 398.7 eV corresponds to the nitrogen atoms bound with three C atoms, N-(C)$_3$, and the peak at 400.0 eV is attributed to C–N–C in the heptazine rings. The peak at 401.2 eV is assigned to the C–N–H bond. The peak at 404.9 eV is assigned to plasmon excitation of the aromatic system of heptazine heterocycles [32,33].
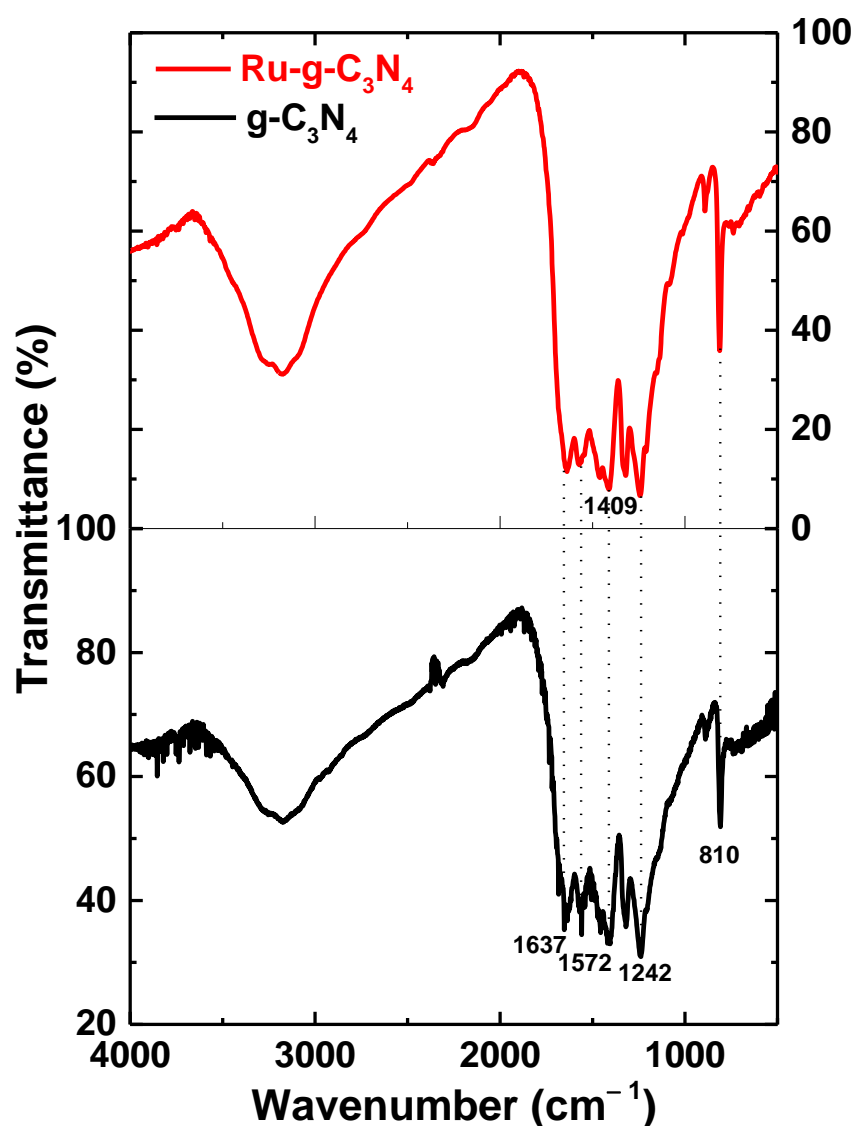
Figure 5. FT-IR spectra of Ru-g-C_3N_4 (red line) and g-C_3N_4 (black line).

The peaks at 530.5 eV and 531.7 eV in the O1s spectra are related to C–O and C=O groups, respectively (Figure 6f). The binding energy at 533.3 eV is assigned to the adsorbed H_2O [9].

The surface atomic concentrations of the Ru/g-C_3N_4 catalyst from the XPS analysis (Table S1 in the Supplementary Materials) show 1.4% ruthenium, which is almost three times higher than that determined by EDS. This deviation originates from the different penetrations of Ru during the impregnation, as well as from the measuring depths of the two techniques (3–10 nm for XPS, 3 μm for EDS). Due to the impregnation method, these concentrations are significantly lower than the theoretical 5%, in the case of which all Ru ions in the solution phase would have been deposited/incorporated.

2.1.6. TEM Analysis

The morphologies of representative material (g-C_3N_4 and Ru/g-C_3N_4) are determined by the TEM analysis technique. The distribution of ruthenium is shown in Figure 7. It is clearly visible that the morphology of the g-C_3N_4 support (Figure 7a,b) prepared by the calcination method was of a lamellar structure. Figure 7c,d illustrate that the active catalyst component Ru exists in the form of nanoparticles (NPs) on the support and the particle size of Ru NPs.
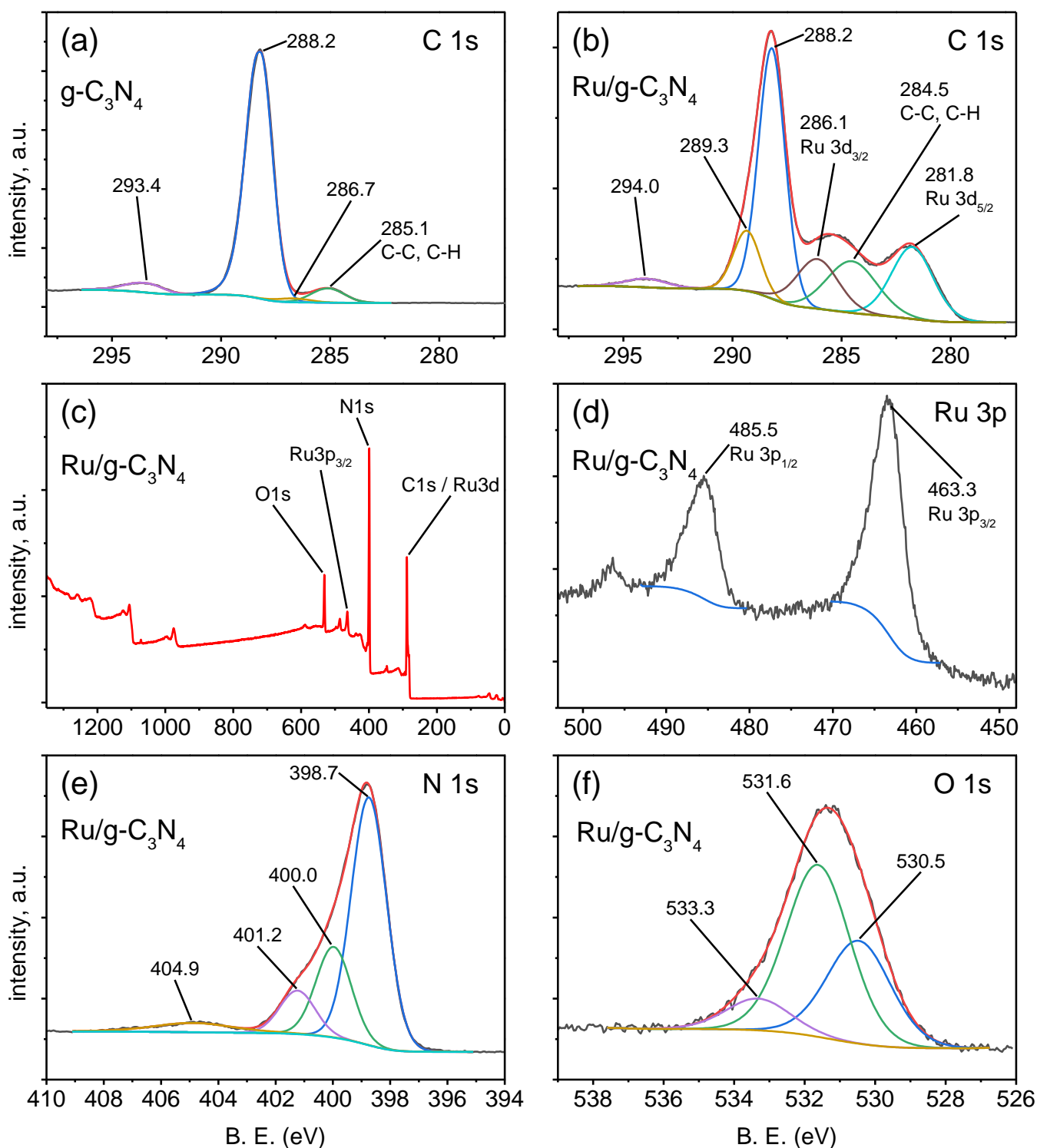
Figure 6. XPS spectra: high resolution XPS spectra in the C1s region of g-C$_3$N$_4$ (**a**) and of Ru/g-C$_3$N$_4$ (**b**); full scan of Ru/g- (**c**) and Ru3p scan of Ru/g-C$_3$N$_4$ (**d**); high resolution XPS spectra in the N1s region (**e**) and O1s region (**f**) of Ru/g-C$_3$N$_4$.

(**a**)

(**b**)

(**c**)

(**d**)
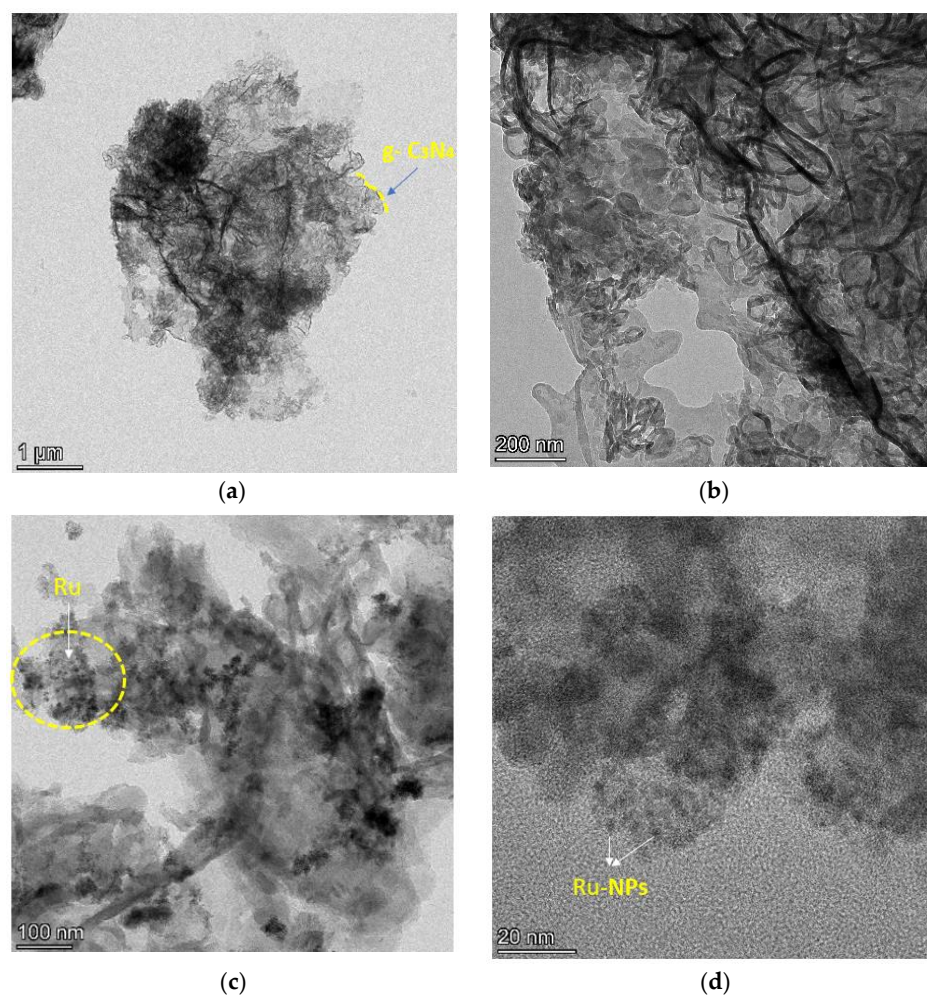
Figure 7. TEM images of g-C$_3$N$_4$ (**a**,**b**) and 5% Ru/g-C$_3$N$_4$ catalysts (**c**,**d**).

2.2. Investigation of Adsorption Equilibrium Time

The absorbance change of the aqueous Cr(VI) over time due to adsorption onto Ru/g-C$_3$N$_4$ is shown in Figure 8. The adsorption equilibrium was achieved after 60 min. It was chosen as the suitable adsorption time for the subsequent photocatalysis experiments.
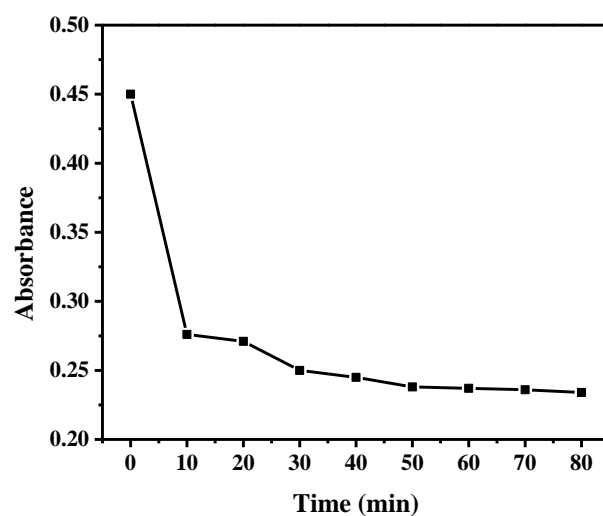

Figure 8. Adsorption of Cr(VI) in the solution (pH 2) onto Ru/g-C$_3$N$_4$.

2.3. Photocatalytic Activity of Ru/g-C₃N₄

Photocatalytic reduction experiments of Cr(VI) over g-C$_3$N$_4$ and Ru/g-C$_3$N$_4$ were performed under visible light irradiation ($\lambda \geq 400$ nm) (Figure 9). The 5% Ru/g-C$_3$N$_4$ composite shows the highest photocatalytic activity, and 96.81% Cr(VI) is reduced after 120 min, which is two times higher than that of pure g-C$_3$N$_4$ (50.1%). Table S2 (in the Supplementary Materials) displays a comparison on Cr(VI) removal by different photocatalytic methods. According to these data, Cr(VI) removal performance by photocatalysis based on Ru/g-C$_3$N$_4$ is comparable to those of other photocatalytic materials [18,20,21,25,38–42].
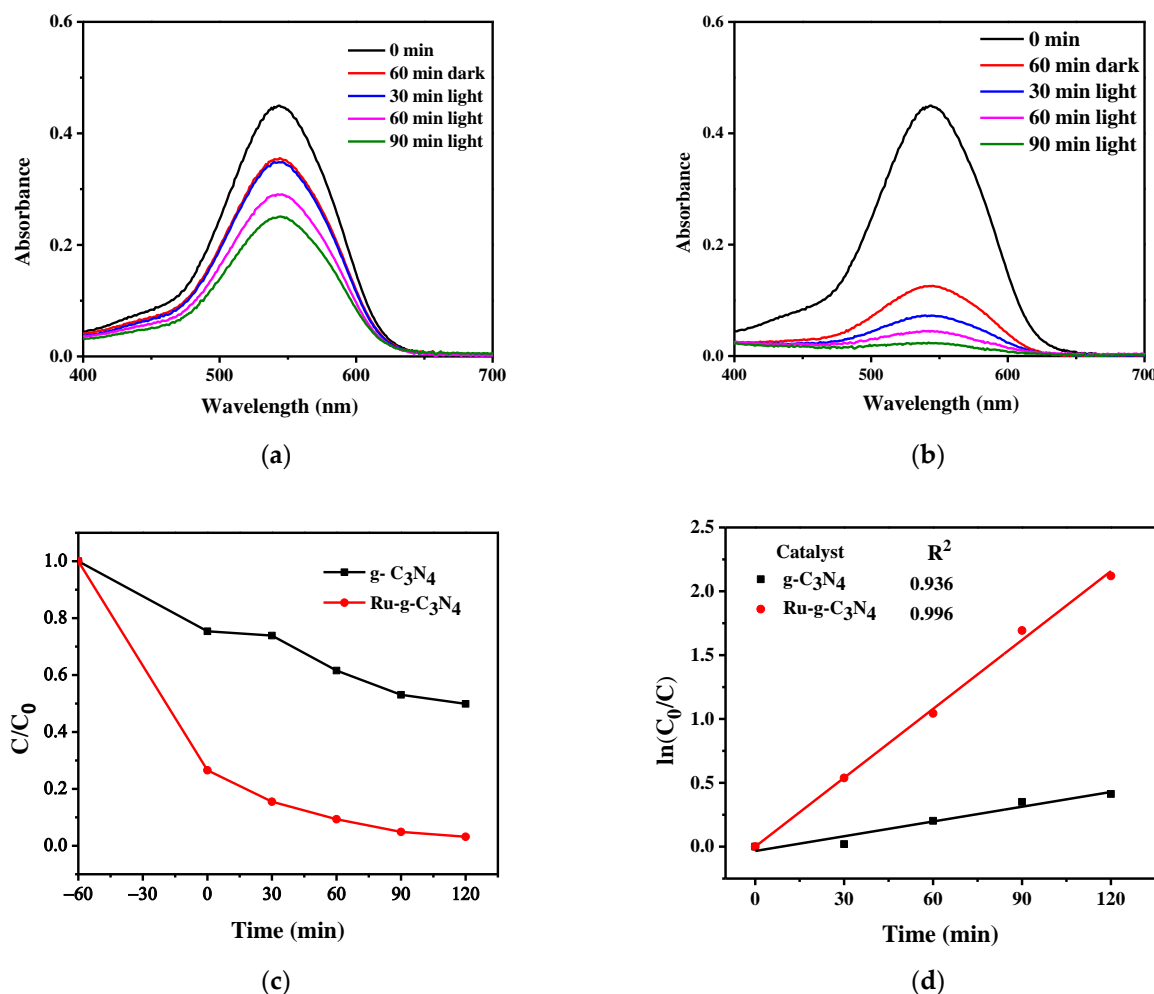

Figure 9. UV–Vis spectra were measured during the treatment of Cr(VI) solution (pH 2) at certain irradiation times using (**a**) g-C$_3$N$_4$ (**b**) Ru/g-C$_3$N$_4$ and kinetic curves (**c**,**d**).

This proves that Ru doping into g-C$_3$N$_4$ gives positive results regarding the efficiency of the photocatalytic Cr(VI) reduction. This result may be attributed to the relation of the CB energies of g-C$_3$N$_4$ and Ru/g-C$_3$N$_4$ as indicated in Section 2.1.2. The very similar E$_{CB}$ values may lead to an equilibrium of the electrons between the two CBs. Hence, Ru/g-C$_3$N$_4$ has a good chance to entrap electrons from the CB of g-C$_3$N$_4$. (Notably, the latter one can be easier excited due to its lower band gap.) As a consequence of electron capturing, the chance for charge recombination is diminished. Additionally, the (even if slightly) more negative CB potential of Ru/g-C$_3$N$_4$ may promote a more efficient Cr(VI) reduction. Figure 10 shows a simplified scheme of the charge-transfer mechanism taking place in the system upon excitation of the g-C$_3$N$_4$ catalyst doped with Ru. On the basis of the XPS analysis, most of the ruthenium in +2 oxidation states are connected to N atoms

through covalent bonds (see in Section 2.1.5.). This mechanism is also supported by the result of scavenging experiments (Section 2.3.4.).
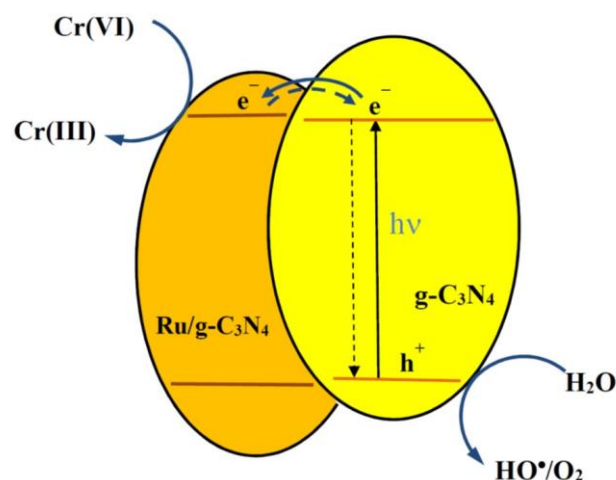

Figure 10. Schematic illustration of the of the charge-transfer mechanism of the photocatalytic Cr(VI) reduction based on g-C$_3$N$_4$ c doped with ruthenium.

2.3.1. Effect of Initial Solution pH

As pH strongly affects the photocatalytic reduction of Cr(VI), the effect of pH was studied in the range 2–10 with Ru/g-C$_3$N$_4$. The optimal pH solution for effective Cr(VI) removal by Ru/g-C$_3$N$_4$ the material was 2 (Figure 11 and Table 2).
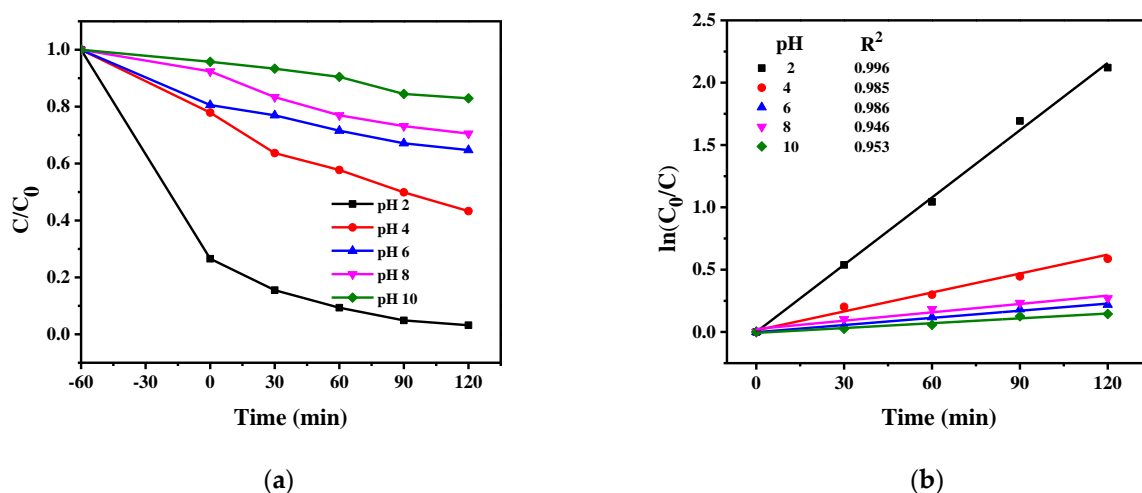

(**a**)

(**b**)

Figure 11. (**a**) Effect of initial pH of the Cr(VI) solution on the photocatalytic efficiency of Ru/g-C$_3$N$_4$ and (**b**) kinetic curves.

Table 2. The conversion of Cr(VI) to Cr(III) during the photocatalytic experiment.

Time (min) *	Initial	0 *	30	60	90	120
chromium species	concentration (ppm) **					
Cr(VI)	20	9.0	5.6	4.5	1.9	1.0
Cr(III)	-	-	4.2	8.7	12.6	12.6
conversion (%)	-	-	43.2	65.8	87.2	92.5

* Time of zero was set as starting illumination (after 60 min equilibrium in dark). ** Cr(VI) concentration was present in the solution. Cr(III) was calculated according to the ref. [43].

In contrast, as the pH is increased, the Cr(VI) removal efficiency by Ru/g-C$_3$N$_4$ material is decreased. This can partly be explained by the surface charge property of the material which also depends on the pH. The pH$_{PZC}$ value of a material is the pH value at which the surface charge is zero. When the pH is lower than the pH$_{PZC}$ value, the catalyst surface becomes positively charged, resulting in better anion adsorption. Similarly, when the pH is higher than the pH$_{PZC}$ value, the surface of the adsorbent carries a negative charge, which will better adsorb the cations [33]. The pH$_{PZC}$ of Ru/g-C$_3$N$_4$ was determined to be 6.59 (Figure 12). It is higher than the isoelectric point of the pristine g-C$_3$N$_4$ (pH$_{ZPC}$ = 4–5 [44]), but the Ru^{2+} species can promote the neutralization of the particle surface already at a lower proton concentration. At low pH, Cr(VI) forms exist as HCrO$_4^-$ and Cr$_2$O$_7^{2-}$; when pH increases, they convert to CrO$_4^{2-}$. Furthermore, at low pH, the surface of the photocatalyst becomes highly protonated, leading to better adsorption of HCrO$_4^-$ or Cr$_2$O$_7^{2-}$. At higher pH, the surface of the photocatalyst becomes more negative, which tends to repel the negatively charged ions and thus decreases the photocatalytic reduction rate of Cr(VI). The other, perhaps even stronger, effect of pH on the reduction of Cr(VI) originates from the dramatic change of the corresponding standard redox potentials: in acidic solution E° (Cr$_2$O$_7^{2-}$/Cr^{3+}) = 1.38 V, in basic solution E° (CrO$_4^{2-}$/Cr(OH)$_3$) = −0.11, or E° (CrO$_4^{2-}$/Cr(OH)$_4^-$) = −0.72. [45]. Hence, at high concentrations of H$^+$ ions, the oxidation potential of Cr(VI) dramatically increases compared to the cases of weakly acidic or neutral systems. Accordingly, the most significant increase in the efficiency of photocatalytic Cr(VI) reduction was observed at the pH change from 4 to 2 (see Figure 11).
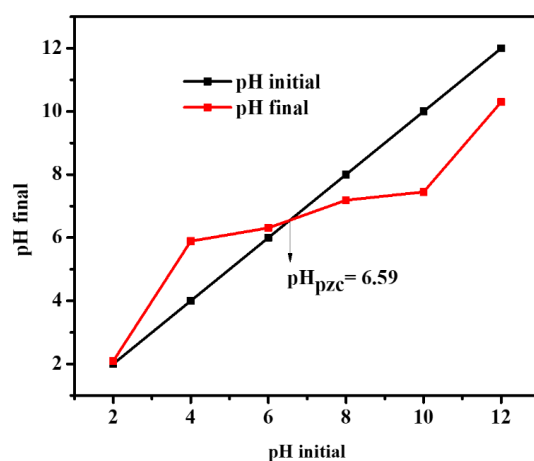

Figure 12. pH$_{pzc}$ determination for Ru/g-C$_3$N$_4$.

2.3.2. Effect of Photocatalyst Concentration

The catalyst content is also one of the factors affecting the Cr(VI) treatment efficiency in water. Experiments were performed by varying the photocatalytic material content with a fixed Cr(VI) concentration (20 ppm) and an optimal pH was selected (pH 2). The amount of material selected is 1 g/L, 2 g/L, and 3 g/L, respectively. The results are shown in Figure 13.

When the material content was increased to 1 g/L, the treatment efficiency increased significantly. However, when increasing to 3 g/L, the processing efficiency tends to decrease. The influence of catalyst mass on the degradation process can be explained by the following reasons: an increase in catalyst mass leads to an increase in the number of active sites available on the catalyst surface, increasing the density of the catalyst particles in the illuminated area; therefore, the photocatalytic ability of the material is better, leading to a rapid increase in Cr(VI) treatment efficiency [33]. However, when the catalyst content increases, it leads to an increase in the density of particles suspended on the surface of the solution, hindering the penetration of light, and increasing the light scattering effect. In addition, when increasing the amount of catalyst added, each catalyst molecule has a reduced chance of contacting Cr^{6+} because of the rapid reaction [46]. As a result, the

efficiency and reaction rate can be improved with increasing catalyst content, but the Cr^{6+} conversion capacity is reduced.
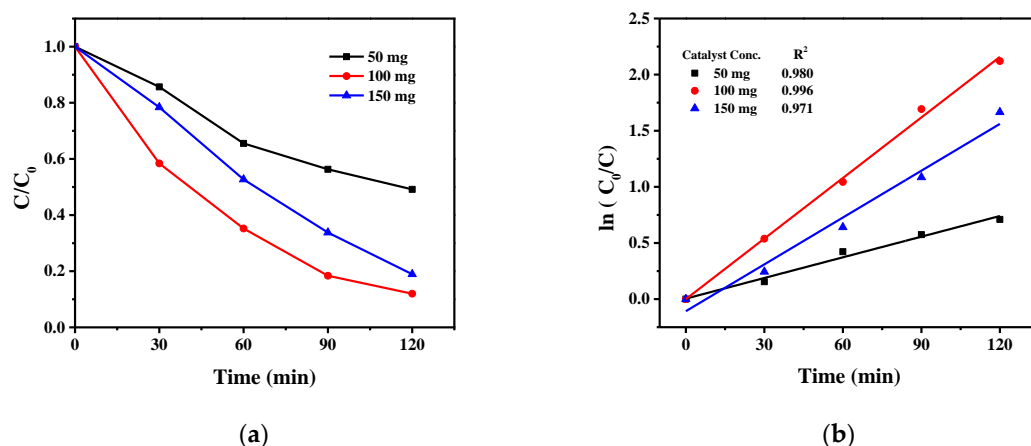

(**a**)   (**b**)

Figure 13. (**a**) Effect of Ru/g-C_3N_4 content on Cr(VI) treatment ability and (**b**) first-order kinetic curves.

2.3.3. Effect of Initial Cr(VI) Concentration

The photocatalytic efficiency of the Ru/g-C_3N_4 catalyst in the reduction of Cr(VI) was investigated at various concentrations (15–100 ppm) of Cr(VI) at an initial solution pH of 2.0, and 0.1 g/L of catalyst with a reaction time of 120 min (Figure 14). The photocatalytic efficiency of the reaction decreased when the initial concentration of Cr(VI) was increased, and drastically reduced with 100 ppm of Cr(VI) (to ca. 10%). This behavior is related to a large amount of Cr(VI) that is adsorbed on the surface of the photocatalyst and prevents the light absorption during the reaction. Hence, under these conditions, the specific and available surface area of the photocatalyst decreased, which resulted in lower photocatalytic efficiency. In this case, even the reaction rate (ppm/min) decreased significantly. However, at concentrations 30 and 50 ppm, the reaction rate increased compared to the case of 15 ppm because the faster capturing of CB electrons by Cr(VI) overcompensated the decreased light absorption. From a comparison based on the product of the initial concentration of Cr(VI) and the $\ln(C/C_0)$ value at 120 min, the highest reaction rate was observed at 50 ppm.
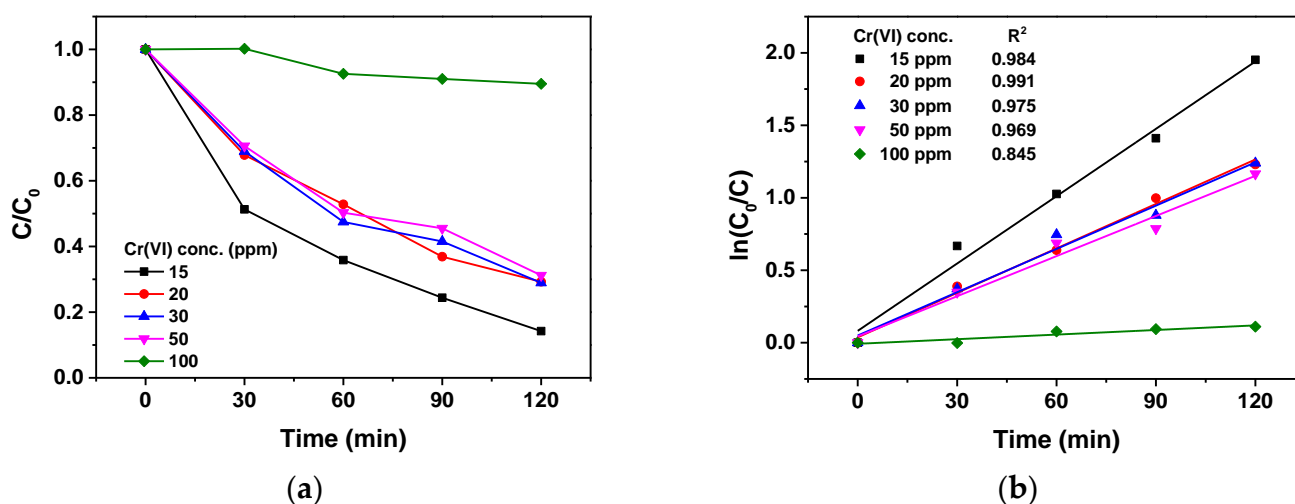

(**a**)   (**b**)

Figure 14. (**a**) Effect of initial Cr(VI) concentration on the photocatalytic efficiency of Ru/g-C_3N_4 and (**b**) first-order kinetic curves.

2.3.4. Scavenging Effect of Coumarin

The mechanism of the photocatalytic Cr(VI) reduction involving a g-C_3N_4-based catalyst has earlier been investigated by application of various scavengers such as formic acid

(for •OH radicals), p-benzoquinone (for superoxide radicals), silver nitrate (for electrons), and isopropanol (for holes) [20]. On the basis of the results of these free radical trapping experiments, it was suggested that the generation of electrons and (in the presence of dissolved oxygen) $O_2^{\bullet-}$ plays a determining role in the primary steps of the photocatalytic reduction of Cr(VI) based on g-C$_3$N$_4$. Since, according to our previous studies, coumarin can efficiently react not only with •OH radicals [47] but with electrons, too [48,49], it was applied as a multifunctional scavenger competing for the primary agents photogenerated by excitation of Ru/g-C$_3$N$_4$. In the presence of coumarin with a concentration of 2.5×10^{-5} M, the Cr(VI) treatment efficiency of Ru/g-C$_3$N$_4$ decreased markedly (Figure 15). The performance reduced from 96.81% to 75.43%. These results indicate that from the two opposite processes (i.e., reaction with •OH radicals or even valence-bond holes, which would promote the reduction of Cr(VI), and capturing conduction-band electrons, which would decrease the efficiency of Cr(III) formation), the latter proved to be predominant. This observation is in accordance with the corresponding reaction rate constants of coumarin 6.4–6.9×10^9 mol^{-1} dm^3 s^{-1} with •OH radical and 1.1–1.7×10^{10} mol^{-1} dm^3 s^{-1} with electron [50,51]). In addition, the shape of the curve regarding the Cr(VI) decay in the presence of coumarin (Figure 13a) indicates that competition for the conduction band electrons significantly hinders the Cr(VI) reduction, especially in the first hour of irradiation.
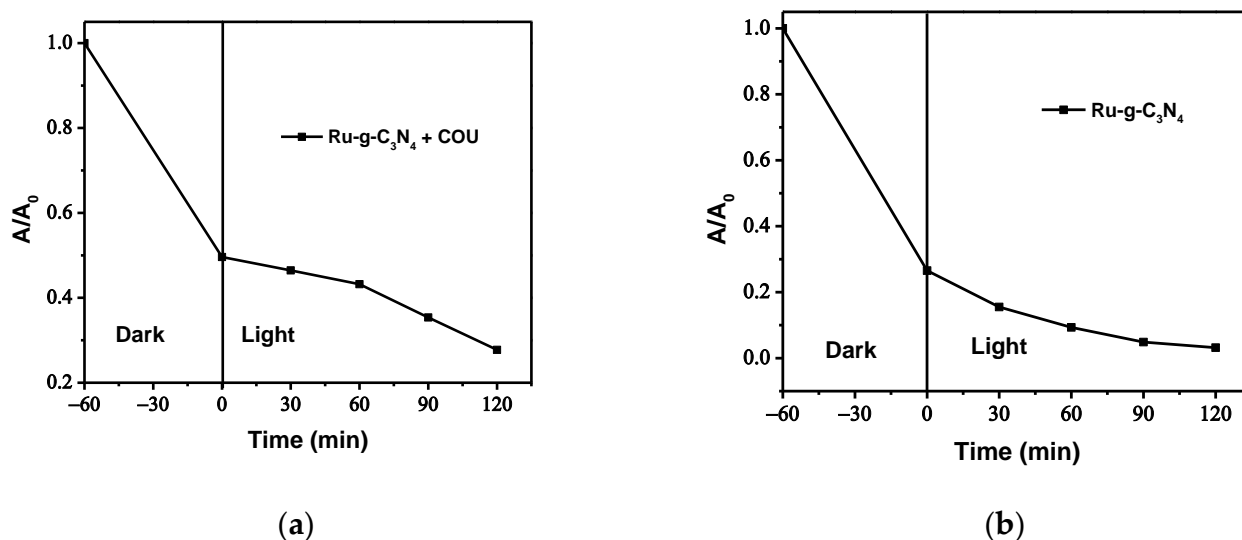

(**a**)   (**b**)

Figure 15. The presence (**a**) and absence (**b**) of coumarin (COU) during photocatalytic reduction of aqueous Cr(VI) (pH 2) by Ru/g-C$_3$N$_4$.

2.3.5. Reusability of the Photocatalyst

The reusability of the Ru/g-C$_3$N$_4$ sample was evaluated regarding its stability over three consecutive cycles (Figure 16). As Figure 16 indicates, the photocatalyst showed almost the same photodegradation activity towards 20 mg L^{-1} K$_2$Cr$_2$O$_7$ solution in all three experiments. A slight decrease in the removal efficiency may be due to a loss of catalyst during the collection after each run. Slight differences in the shape of the plot in the case second and third runs compared to the first one may probably arise from a temporary decrease of the active sites on the surface of the Ru/g-C$_3$N$_4$ catalyst during its collection after each run. As a consequence, the adsorption–desorption property of the reused catalyst may slightly deviate from that of the fresh one. In the second period of the irradiations, however, a regeneration of the active sites took place; therefore, no significant decrease could be observed in the photocatalytic yield after three recycling experiments, indicating the stability of the catalyst.
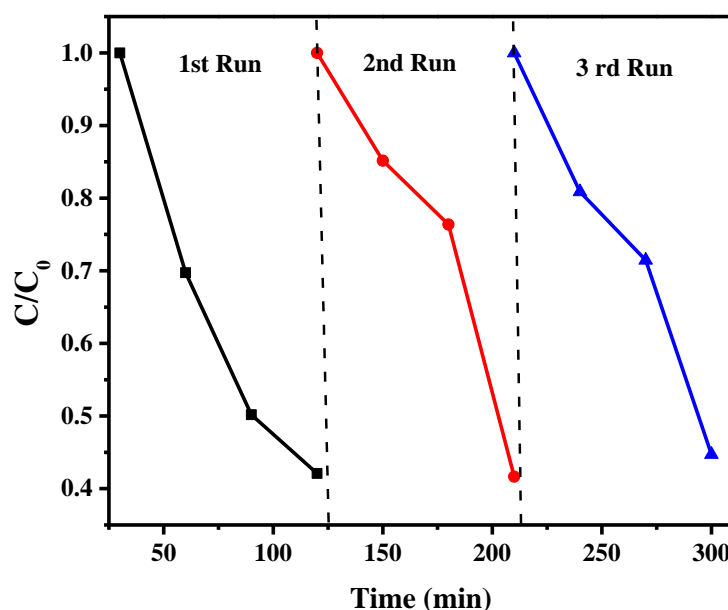
Figure 16. Recycle experiments of the photocatalytic reduction of Cr(VI) solution (pH 2) using 5% Ru/g-C$_3$N$_4$.

3. Materials and Methods

3.1. Materials

Thiourea (CH$_4$N$_2$S, 99%) and ruthenium (III) chloride (RuCl$_3$.xH$_2$O, 99%) were purchased from Merck, Darmstadt, Germany. Sodium borohydride (NaBH$_4$, 98%), ethanol (C$_2$H$_5$OH, 99.7%), and potassium dichromate (K$_2$Cr$_2$O$_7$, 99%) were obtained from GHTech, Guangzhou, China.

3.2. Catalyst Preparation

3.2.1. Preparation of g-C$_3$N$_4$ Catalyst

The g-C$_3$N$_4$ catalyst was synthesized by a simple calcination method: 3 g of thiourea in a porcelain crucible with a cover. For the calcination process, the sample was heated 25 to 550 °C at 2 °C min^{-1} for 4 h. At the end of the heating process, the crucible was cooled down to room temperature, and the solid sample of g-C$_3$N$_4$ was ground to powder and collected [52]. Samples are stored in vials and labeled with sample g-C$_3$N$_4$. The sample synthesis process and the schematic for plausible intermediates at different temperature ranges have been shown in Figure 17. Notably, the g-C$_3$N$_4$ can be synthesized by hydrothermal condensation from melamine or other triazine precursors, too. However, it was reported that the g-C$_3$N$_4$ synthesized from thiourea, a sulfur-containing precursor, could take advantage of a sulfur-mediated process, which improved the degree of polycondensation and polymerization of g-C$_3$N$_4$, thus enhancing the energy conversion efficiency [53].

3.2.2. Preparation of Ru/g-C$_3$N$_4$ Catalyst

The Ru/g-C$_3$N$_4$ catalyst was synthesized by a simple method of ultrasonic impregnation. Initially, 0.95g g-C$_3$N$_4$ was evenly dispersed in 34 mL H$_2$O in a beaker, then 30 mL RuCl$_3$ aqueous solution with a concentration of 0.01 g mL^{-1} was added to the beaker. Subsequently, after ultrasound treatment for 60 min, 5 mL deionized water containing 300 mg NaBH$_4$ was added to the solution and kept the solution in ultrasound for another 120 min [52]. The solution was then filtered and washed several times with distilled water and alcohol to remove impurities. The material was dried at 110 °C for 16 h, finally obtaining a black material with the symbol 5% Ru/g-C$_3$N$_4$.
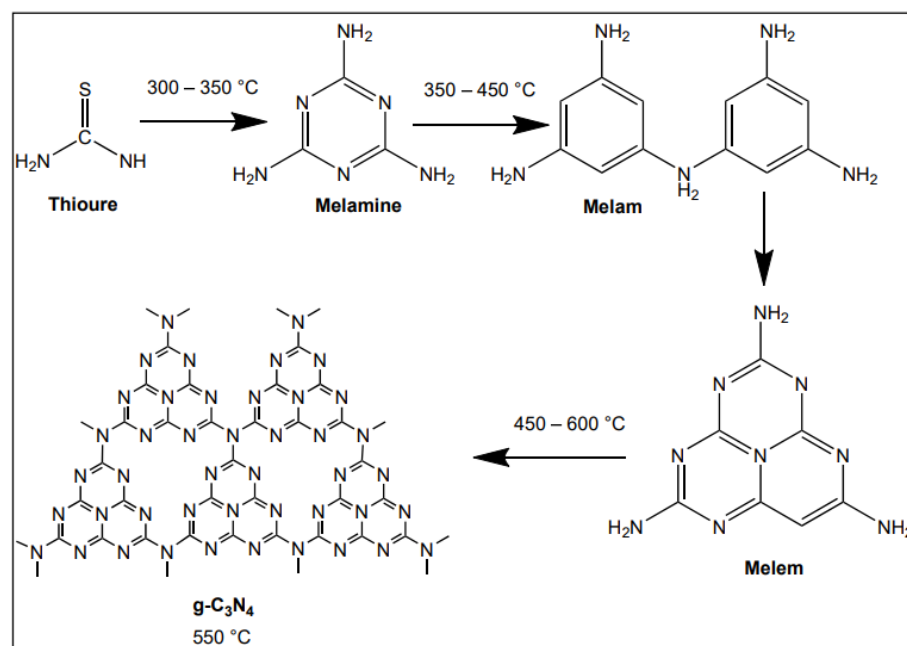
Figure 17. Schema for the synthesis of g-C$_3$N$_4$, showing the plausible intermediates at different temperature ranges.

3.3. Sample Characterization

The prepared samples were characterized by X-ray diffraction (XRD, Malvern PANalytical, Aeris, Almelo, The Netherlands), Fourier transform infrared spectroscopy (FT-IR, Shimadzu, IRAffinity-1S, Kyoto, Japan), scanning electron microscopy (SEM, NanoSEM 450 FEI, Eindhoven, The Netherlands) equipped with a TEAM Apollo XL energy dispersive spectroscopy (Britain EDAX Co., Ltd., Cambridge, UK), diffuse reflectance UV–Visible spectroscopy (DR/UV–Vis, Carry 5000 UV–Vis-NIR, Santa Clara, CA, USA), and UV–Vis spectrophotometry (Agilent 8453, Santa Clara, CA, USA).

The elemental composition and chemical state analysis of sample surfaces have been carried out by XPS, on a Thermo Scientific ESCALAB Xi$^+$ instrument (assembled in Brno, Czech Republic). A monochromatized Al K-alpha source (1486.6 eV), with a 650 μm spot size was used. The pressure of the analysis chamber was lower than 10^{-9} mbar before conducting the experiment. On each sample, a wide range of spectra were collected (at analyzer pass energy of 80 eV) for surveying the elemental composition. For quantitative and chemical state analysis, high-resolution spectra (at 40 eV pass energy) were recorded for the following photoelectron lines: C 1s, Ru 3d, N 1s, O 1s, Ru 3p, Ca 2p, and Na 1s regions. The charging of the sample surface was compensated for by using the automatic built-in charge compensation system. The energy of sp^2-bonded C in N=C(–N)$_2$, set at 288.2 eV was used as the internal reference for fine energy scale adjustment.

Samples for transmission electron microscopy (TEM) were prepared by depositing a drop of diluted aqueous suspension of the original samples on copper TEM grids covered by continuous carbon amorphous support film. TEM analyses were performed using a Talos F200X G2 instrument (Thermo Fisher Scientific, Waltham, MA, USA), operated at 200 kV accelerating voltage, equipped with a field emission gun and a four-detector Super-X energy-dispersive X-ray spectrometer (Termo Fisher Scientific), and capable of working in both conventional TEM and scanning transmission (STEM) modes. In our study, TEM bright-field images, HRTEM images, and STEM high-angle annular dark-field (HAADF) images were collected to visualize the crystal size, and the morphology of the particles, and HRTEM images as well as electron diffraction patterns were used to study the structural properties. STEM-EDS elemental maps were collected to measure and visualize the chemical compositions.

3.4. Photocatalytic Reduction Experiments

The photocatalytic activity of the as-prepared samples, g-C_3N_4 and Ru/g-C_3N_4, was evaluated, which was assessed through the reductive efficiency of aqueous Cr(VI) to Cr(III) under the illumination with a 500W Hg-lamp through a cut-off filter transmitting $\lambda \geq 400$ nm. The reaction was carried out at room temperature, in a glass double-shell reactor containing 50 mL of Cr(VI) solution (20.0 mg/L) and 0.1 g of photocatalyst. Prior to the light irradiation, the mixture was dispersed by sonication for 3 min and kept for stirring at 250 rpm for 60 min in the dark to attain the adsorption–desorption equilibrium. At regular intervals, 2 mL of the suspension was aspirated during irradiation and filtered with a syringe filter (0.45 μm nylon membrane) for immediate photocatalyst separation. The diphenylcarbazide was used as a reagent to analyze Cr(VI) concentration by UV–Vis spectrophotometry, observed at 540 nm by a spectrophotometer (Agilent 8453, Santa Clara, CA, USA) [54].

4. Conclusions

Ruthenium doping of g-C_3N_4 prepared from thiourea proved to be a successful method for a significant enhancement of the efficiency of photocatalytic reduction of Cr(VI) based on this catalyst. According to the XPS analysis, most of the ruthenium incorporated by impregnation was mostly in oxidation state +2 and bound to the N atoms on or close to the surface of the catalyst particles. This modification can diminish the recombination of the charge carriers formed upon excitation of the photoactive semiconductor and, thus, increase the efficacy of the Cr(VI) reduction with CB electrons. pH 2 was found to be optimal for the photocatalytic reaction because of the advantageous surface charge and E(Cr(VI)/Cr(III)) redox potential. The performance of the Ru/g-C_3N_4 catalyst was stable after several cycles of reuse, and its efficiency was comparable with those of other photocatalysts developed for Cr(VI) reduction. Hence, Ru-doped g-C_3N_4 may be a promising photocatalyst for this purpose, and maybe for other reductive processes, too.

Author Contributions: Conceptualization, T.N.X.; methodology, T.N.X. and O.H.; software, T.N.X.; validation, D.N.T., T.N.N., K.D.Q. and M.N.; formal analysis, T.N.X., O.H.; investigation, D.N.T., T.N.N., K.D.Q., M.N. and S.M.; resources, T.N.X. and O.H.; data curation, D.N.T., T.N.N., K.D.Q., M.N. and S.M.; writing—original draft preparation, T.N.X. and O.H.; writing—review and editing, T.N.X., M.N. and O.H.; visualization, T.N.X. and O.H.; supervision, T.N.X. and O.H.; project administration, T.N.X. and O.H.; funding acquisition, T.N.X. and O.H. All authors have read and agreed to the published version of the manuscript.

Data Availability Statement: The data presented in this study are available on request from the corresponding author. The data are not publicly available due to privacy.

Conflicts of Interest: The authors declare no conflict of interest.

References

1. Wang, H.; Li, X.; Zhao, X.; Li, C.; Song, X.; Zhang, P.; Huo, P. A review on heterogeneous photocatalysis for environmental remediation: From semiconductors to modification strategies. *Chin. J. Catal.* **2022**, *43*, 178–214. [CrossRef]
2. Chen, Y.; Li, A.; Li, Q.; Hou, X.; Wang, L.-N.; Huang, Z.-H. Facile fabrication of three-dimensional interconnected nanoporous N-TiO$_2$ for efficient photoelectrochemical water splitting. *J. Mater. Sci. Technol.* **2018**, *34*, 955–960. [CrossRef]
3. Dong, J.; Zhang, Y.; Hussain, M.I.; Zhou, W.; Chen, Y.; Wang, L.-N. g-C$_3$N$_4$: Properties, Pore Modifications, and Photocatalytic Applications. *Nanomaterials* **2021**, *12*, 121. [CrossRef]
4. Liang, Q.; Li, Z.; Yu, X.; Huang, Z.-H.; Kang, F.; Yang, Q.-H. Macroscopic 3D Porous Graphitic Carbon Nitride Monolith for Enhanced Photocatalytic Hydrogen Evolution. *Adv. Mater.* **2015**, *27*, 4634–4639. [CrossRef] [PubMed]
5. Wen, J.; Xie, J.; Yang, Z.; Shen, R.; Li, H.; Luo, X.; Chen, X.; Li, X. Fabricating the Robust g-C$_3$N$_4$ Nanosheets/Carbons/NiS Multiple Heterojunctions for Enhanced Photocatalytic H$_2$ Generation: An Insight into the Trifunctional Roles of Nanocarbons. *ACS Sustain. Chem. Eng.* **2017**, *5*, 2224–2236. [CrossRef]
6. Yang, Y.; Zhang, C.; Huang, D.; Zeng, G.; Huang, J.; Lai, C.; Zhou, C.; Wang, W.; Guo, H.; Xue, W.; et al. Boron nitride quantum dots decorated ultrathin porous g-C$_3$N$_4$: Intensified exciton dissociation and charge transfer for promoting visible-light-driven molecular oxygen activation. *Appl. Catal. B Environ.* **2019**, *245*, 87–99. [CrossRef]
7. Li, Y.; Liu, Z.; Li, Z.; Wang, Q. Renewable biomass-derived carbon-supported g-C$_3$N$_4$ doped with Ag for enhanced photocatalytic reduction of CO$_2$. *J. Colloid Interface Sci.* **2022**, *606*, 1311–1321. [CrossRef]
8. Kumar, A.; Kashyap, S.; Sharma, M.; Krishnan, V. Tuning the surface and optical properties of graphitic carbon nitride by incorporation of alkali metals (Na, K, Cs and Rb): Effect on photocatalytic removal of organic pollutants. *Chemosphere* **2022**, *287*, 131988. [CrossRef]
9. Wang, Y.; Wang, H.; Chen, F.; Cao, F.; Zhao, X.; Meng, S.; Cui, Y. Facile synthesis of oxygen doped carbon nitride hollow microsphere for photocatalysis. *Appl. Catal. B Environ.* **2017**, *206*, 417–425. [CrossRef]
10. Guo, S.; Tang, Y.; Xie, Y.; Tian, C.; Feng, Q.; Zhou, W.; Jiang, B. P-doped tubular g-C$_3$N$_4$ with surface carbon defects: Universal synthesis and enhanced visible-light photocatalytic hydrogen production. *Appl. Catal. B Environ.* **2017**, *218*, 664–671. [CrossRef]
11. Tian, B.; Wu, Y.; Lu, G. Metal-free plasmonic boron phosphide/graphitic carbon nitride with core-shell structure photocatalysts for overall water splitting. *Appl. Catal. B Environ.* **2021**, *280*, 119410. [CrossRef]
12. Zhao, H.; Jiang, Z.; Xiao, K.; Sun, H.; Chan, H.S.; Tsang, T.H.; Yang, S.; Wong, P.K. Photo-assisted separation of noble-metal-free oxidation and reduction cocatalysts for graphitic carbon nitride nanosheets with efficient photocatalytic hydrogen evolution. *Appl. Catal. B Environ.* **2021**, *280*, 119456. [CrossRef]
13. Gu, J.; Guo, R.; Miao, Y.; Liu, Y.; Wu, G.; Duan, C.; Pan, W. Construction of full spectrum-driven Cs$_x$WO$_3$/g-C$_3$N$_4$ heterojunction catalyst for efficient photocatalytic CO$_2$ reduction. *Appl. Surf. Sci.* **2021**, *540*, 148316. [CrossRef]
14. Liu, R.; Bie, Y.; Qiao, Y.; Liu, T.; Song, Y. Design of g-C$_3$N$_4$/TiO$_2$ nanotubes heterojunction for enhanced organic pollutants degradation in waste water. *Mater. Lett.* **2019**, *251*, 126–130. [CrossRef]
15. Niu, Q.; Liu, M.; Fang, L.; Yu, Y.; Cheng, L.; You, T. Highly dispersed and stable nano zero-valent iron doped electrospun carbon nanofiber composite for aqueous hexavalent chromium removal. *RSC Adv.* **2022**, *12*, 8178–8187. [CrossRef] [PubMed]
16. Türkmen, D.; Bakhshpour, M.; Akgönüllü, S.; Aşır, S.; Denizli, A. Heavy Metal Ions Removal from Wastewater Using Cryogels: A Review. *Front. Sustain.* **2022**, *3*, 765592. [CrossRef]
17. Liang, J.; Jing, C.; Wang, J.; Men, Y. Photocatalytic Reduction of Cr(VI) over g-C$_3$N$_4$ Photocatalysts Synthesized by Different Precursors. *Molecules* **2021**, *26*, 7054. [CrossRef]
18. Sun, H.; Wang, L.; Liu, Y.; Cheng, Z.; Zhao, Y.; Guo, H.; Qu, G.; Wang, T.; Yin, X. Photocatalytic reduction of Cr(VI) via surface modified g-C$_3$N$_4$ by acid-base regulation. *J. Environ. Manag.* **2022**, *324*, 116431. [CrossRef]
19. Niu, X.; Dong, J.; Wang, X.L.; Yao, Y.-F. Enhanced photocatalytic reduction of Cr(VI) to Cr(III) over g-C$_3$N$_4$ catalysts with Ag nanoclusters in conjunction with Cr(III) quantification based on operando low-field NMR relaxometry. *Environ. Sci. Nano* **2020**, *7*, 2823–2832. [CrossRef]
20. Wang, Y.; Bao, S.; Liu, Y.; Yang, W.; Yu, Y.; Feng, M.; Li, K. Efficient photocatalytic reduction of Cr(VI) in aqueous solution over CoS$_2$/g-C$_3$N$_4$-rGO nanocomposites under visible light. *Appl. Surf. Sci.* **2020**, *510*, 145495. [CrossRef]
21. Ajiboye, T.O.; Oyewo, O.A.; Marzouki, R.; Onwudiwe, D.C. Photocatalytic Reduction of Hexavalent Chromium Using Cu$_{3.21}$Bi$_{4.79}$S$_9$/g-C$_3$N$_4$ Nanocomposite. *Catalysts* **2022**, *12*, 1075. [CrossRef]
22. Ding, L.; Deng, Y.; Liu, X.; Liu, L.; Ding, J.; Deng, F. Photocatalytic Reduction of Cr(VI) and Degradation of Organic Pollutants by Z-Scheme g-C$_3$N$_4$/Bi$_2$S$_3$ Heterojunction. *J. Chem. Eng. Res. Updat.* **2022**, *9*, 1–12. [CrossRef]
23. Hu, J.; Lu, S.; Ma, J.; Zhu, F.; Komarneni, S. Composite of g-C$_3$N$_4$/ZnIn$_2$S$_4$ for efficient adsorption and visible light photocatalytic reduction of Cr(VI). *Environ. Sci. Pollut. Res.* **2022**, *29*, 76404–76416. [CrossRef]
24. Sun, H.; Wang, L.; Zhang, Y.; Wang, T.; Yin, X. Photocatalytic reduction performance and mechanisms of Cr(VI) by illite-g-C$_3$N$_4$ under visible light. *Appl. Surf. Sci.* **2023**, *608*, 155226. [CrossRef]
25. Dai, B.; Li, Y.; Xu, J.; Sun, C.; Li, S.; Zhao, W. Photocatalytic oxidation of tetracycline, reduction of hexavalent chromium and hydrogen evolution by Cu$_2$O/g-C$_3$N$_4$ S-scheme photocatalyst: Performance and mechanism insight. *Appl. Surf. Sci.* **2022**, *592*, 153309. [CrossRef]
26. Dong, F.; Wu, L.; Sun, Y.; Fu, M.; Wu, Z.; Lee, S.C. Efficient synthesis of polymeric g-C$_3$N$_4$ layered materials as novel efficient visible light driven photocatalysts. *J. Mater. Chem.* **2011**, *21*, 15171. [CrossRef]

27. Hong, Y.; Liu, E.; Shi, J.; Lin, X.; Sheng, L.; Zhang, M.; Wang, L.; Chen, J. A direct one-step synthesis of ultrathin g-C_3N_4 nanosheets from thiourea for boosting solar photocatalytic H_2 evolution. *Int. J. Hydrogen Energy* **2019**, *44*, 7194–7204. [CrossRef]

28. Pattnaik, S.; Rai, V.K. Insight into the spectroscopic and thermometric properties of titanate phosphors via a novel co-excited laser system. *Mater. Sci. Eng. B* **2021**, *272*, 115318. [CrossRef]

29. Sharma, P.; Sasson, Y. A photoactive catalyst Ru–g-C_3N_4 for hydrogen transfer reaction of aldehydes and ketones. *Green Chem.* **2017**, *19*, 844–852. [CrossRef]

30. Li, L.; Yu, Y.; Lin, S.; Chu, W.; Sun, D.; Su, Q.; Ma, S.; Du, G.; Xu, B. Single ruthenium atom supported on g-C_3N_4 as an efficient photocatalyst for nitrogen fixation in ultra-pure water. *Catal. Commun.* **2021**, *153*, 106294. [CrossRef]

31. Dong, F.; Li, Y.; Wang, Z.; Ho, W.-K. Enhanced visible light photocatalytic activity and oxidation ability of porous graphene-like g-C_3N_4 nanosheets via thermal exfoliation. *Appl. Surf. Sci.* **2015**, *358*, 393–403. [CrossRef]

32. Raevskaya, A.E.; Panasiuk, Y.V.; Korzhak, G.V.; Stroyuk, O.L.; Kuchmiy, S.Y.; Dzhagan, V.M.; Zahn, D.R.T. Photocatalytic H_2 production from aqueous solutions of hydrazine and its derivatives in the presence of nitric-acid-activated graphitic carbon nitride. *Catal. Today* **2017**, *284*, 229–235. [CrossRef]

33. Wang, H.; Li, X.; Ruan, Q.; Tang, J. Ru and RuO_x decorated carbon nitride for efficient ammonia photosynthesis. *Nanoscale* **2020**, *12*, 12329–12335. [CrossRef] [PubMed]

34. Folkesson, B.; Bjorøy, M.; Pappas, J.; Skaarup, S.; Aaltonen, R.; Swahn, C.-G. ESCA Studies on the Charge Distribution in Some Dinitrogen Complexes of Rhenium, Iridium, Ruthenium, and Osmium. *Acta Chem. Scand.* **1973**, *27*, 287–302. [CrossRef]

35. Shepherd, R.E.; Proctor, A.; Henderson, W.W.; Myser, T.K. Assessment of the .pi.-acceptor capability of selected ligands based on the photoelectron spectra of ruthenium ammine complexes. *Inorg. Chem.* **1987**, *26*, 2440–2444. [CrossRef]

36. Sharma, P.; Kumar, S.; Tomanec, O.; Petr, M.; Zhu Chen, J.; Miller, J.T.; Varma, R.S.; Gawande, M.B.; Zbořil, R. Carbon Nitride-Based Ruthenium Single Atom Photocatalyst for CO_2 Reduction to Methanol. *Small* **2021**, *17*, 2006478. [CrossRef]

37. Crist, B.V. *Handbooks of Monochromatic XPS Spectra, Volume 2—Handbook of Commercially Pure Binary Oxides*; XPS International, LLC: Mountain View, CA, USA, 2019; ISBN 978-0-471-49265-8.

38. Ajiboye, T.O.; Imade, E.E.; Oyewo, O.A.; Onwudiwe, D.C. Silver functionalized g-C_3N_4: Photocatalytic potency for chromium(VI) reduction, and evaluation of the antioxidant and antimicrobial properties. *J. Photochem. Photobiol. A Chem.* **2022**, *432*, 114107. [CrossRef]

39. Yang, L.; Zheng, L.; Chen, Z.; Han, J.; Wei, Z.; Lu, M.; Ma, T.; Zhang, S. An All-in-One Photocatalyst: Photocatalytic Reduction of Cr(VI) and Anchored Adsorption of Cr(III) Over Mesoporous Titanium-Sulfonated Carbon Hollow Hemispheres. *J. Environ. Chem. Eng.* **2022**, *10*, 107864. [CrossRef]

40. Zahid, Z.; Rauf, A.; Javed, M.; Alhujaily, A.; Iqbal, S.; Amjad, A.; Arif, M.; Hussain, S.; Bahadur, A.; Awwad, N.S.; et al. Photocatalytic Reduction of Cr(VI) to Cr(III) and Photocatalytic Degradation of Methylene Blue and Antifungal Activity of Ag/TiO_2 Composites Synthesized via the Template Induced Route. *Inorganics* **2023**, *11*, 133. [CrossRef]

41. Wang, X.; Li, L.; Meng, J.; Xia, P.; Yang, Y.; Guo, Y. Enhanced simulated sunlight photocatalytic reduction of an aqueous hexavalent chromium over hydroxyl-modified graphitic carbon nitride. *Appl. Surf. Sci.* **2020**, *506*, 144181. [CrossRef]

42. Chen, X.; Zhang, Y.; Yuan, D.; Huang, W.; Ding, J.; Wan, H.; Dai, W.-L.; Guan, G. One step method of structure engineering porous graphitic carbon nitride for efficient visible-light photocatalytic reduction of Cr(VI). *J. Mater. Sci. Technol.* **2021**, *71*, 211–220. [CrossRef]

43. Wiryawan, A.; Retnowati, R.; Burhan, P.; Syekhfani, S. Method of analysis for determination of the chromium (Cr) species in water samples by spectrophotometry with diphenylcarbazide. *J. Environ. Eng. Sustain. Technol.* **2018**, *5*, 37–46.

44. Zhu, B.; Xia, P.; Ho, W.; Yu, J. Isoelectric point and adsorption activity of porous g-C_3N_4. *Appl. Surf. Sci.* **2015**, *344*, 188–195. [CrossRef]

45. Shriver, D.; Weller, M.; Overton, T.; Rourke, J.; Armstrong, F. *Inorganic Chemistry*, 6th ed.; W. H. Freeman and Co.: New York, NY, USA, 2014; ISBN 978-1-4292-9906-0.

46. Wu, C.; Irshad, F.; Luo, M.; Zhao, Y.; Ma, X.; Wang, S. Ruthenium Complexes Immobilized on an Azolium Based Metal Organic Framework for Highly Efficient Conversion of CO_2 into Formic Acid. *ChemCatChem* **2019**, *11*, 1256–1263. [CrossRef]

47. Czili, H.; Horváth, A. Applicability of coumarin for detecting and measuring hydroxyl radicals generated by photoexcitation of TiO_2 nanoparticles. *Appl. Catal. B Environ.* **2008**, *81*, 295–302. [CrossRef]

48. Wafi, A.; Szabó-Bárdos, E.; Horváth, O.; Makó, É.; Jakab, M.; Zsirka, B. Coumarin-based quantification of hydroxyl radicals and other reactive species generated on excited nitrogen-doped TiO_2. *J. Photochem. Photobiol. A Chem.* **2021**, *404*, 112913. [CrossRef]

49. Wafi, A.; Szabó-Bárdos, E.; Horváth, O.; Pósfai, M.; Makó, É.; Juzsakova, T.; Fónagy, O. The Photocatalytic and Antibacterial Performance of Nitrogen-Doped TiO_2: Surface-Structure Dependence and Silver-Deposition Effect. *Nanomaterials* **2020**, *10*, 2261. [CrossRef]

50. Singh, T.S.; Madhava Rao, B.; Mohan, H.; Mittal, J.P. A pulse radiolysis study of coumarin and its derivatives. *J. Photochem. Photobiol. A Chem.* **2002**, *153*, 163–171. [CrossRef]

51. Náfrádi, M.; Farkas, L.; Alapi, T.; Hernádi, K.; Kovács, K.; Wojnárovits, L.; Takács, E. Application of coumarin and coumarin-3-carboxylic acid for the determination of hydroxyl radicals during different advanced oxidation processes. *Radiat. Phys. Chem.* **2020**, *170*, 108610. [CrossRef]

52. Cao, J.; Han, F.; Wang, L.; Huang, X.; Cao, Y.; He, P.; Yang, H.; Chen, J.; Li, H. Ru/g-C_3N_4 as an efficient catalyst for selective hydrogenation of aromatic diamines to alicyclic diamines. *RSC Adv.* **2020**, *10*, 16515–16525. [CrossRef]

53. Ong, W.-J.; Tan, L.-L.; Ng, Y.H.; Yong, S.-T.; Chai, S.-P. Graphitic Carbon Nitride (g-C$_3$N$_4$)-Based Photocatalysts for Artificial Photosynthesis and Environmental Remediation: Are We a Step Closer To Achieving Sustainability? *Chem. Rev.* **2016**, *116*, 7159–7329. [CrossRef] [PubMed]

54. Xiao, D.; Dai, K.; Qu, Y.; Yin, Y.; Chen, H. Hydrothermal synthesis of α-Fe$_2$O$_3$/g-C$_3$N$_4$ composite and its efficient photocatalytic reduction of Cr(VI) under visible light. *Appl. Surf. Sci.* **2015**, *358*, 181–187. [CrossRef]